Optical bistability with a repulsive optical force in coupled silicon photonic crystal membranes

Pui-Chuen Hui, David Woolf, Eiji Iwase, Young-Ik Sohn, Daniel Ramos, Mughees Khan, Alejandro W. Rodriguez, Steven G. Johnson, Federico Capasso, and Marko Loncar

View Online   **Export Citation**   **CrossMark**

ARTICLES YOU MAY BE INTERESTED IN

Applications of cavity optomechanics
Applied Physics Reviews **1**, 031105 (2014); https://doi.org/10.1063/1.4896029

Optimized optomechanical crystal cavity with acoustic radiation shield
Applied Physics Letters **101**, 081115 (2012); https://doi.org/10.1063/1.4747726

Observation of femtojoule optical bistability involving Fano resonances in high-Q/V_m silicon photonic crystal nanocavities
Applied Physics Letters **91**, 051113 (2007); https://doi.org/10.1063/1.2757607

Optical bistability with a repulsive optical force in coupled silicon photonic crystal membranes

Pui-Chuen Hui,[1] David Woolf,[1] Eiji Iwase,[2] Young-Ik Sohn,[1] Daniel Ramos,[1] Mughees Khan,[3] Alejandro W. Rodriguez,[1,4] Steven G. Johnson,[4] Federico Capasso,[1] and Marko Loncar[1,a)]

[1]School of Engineering and Applied Sciences, Harvard University, Cambridge, Massachusetts 02138, USA
[2]Department of Applied Mechanics and Aerospace Engineering, Waseda University, Tokyo 169-8555, Japan
[3]Wyss Institute for Biologically Inspired Engineering, Harvard University, Boston, Massachusetts 02115, USA
[4]Department of Mathematics, Massachusetts Institute of Technology, Cambridge, Massachusetts 02139, USA

We demonstrate actuation of a silicon photonic crystal membrane with a repulsive optical gradient force. The extent of the static actuation is extracted by examining the optical bistability as a combination of the optomechanical, thermo-optic, and photo-thermo-mechanical effects using coupled-mode theory. Device behavior is dominated by a repulsive optical force which results in displacements of ≈ 1 nm/mW. By employing an extended guided resonance which effectively eliminates multi-photon thermal and electronic nonlinearities, our silicon-based device provides a simple, non-intrusive solution to extending the actuation range of micro-electromechanical devices. © 2013 AIP Publishing LLC. [http://dx.doi.org/10.1063/1.4813121]

Rapid developments in the field of optomechanics have opened up avenues for fundamental research on quantum state manipulation with macroscopic structures[1] and show promise for optomechanical sensors[2] and technologies for both radio-frequency[3] and telecom applications.[4] While most attention has been devoted to compact structures featuring low (picogram) mass and ultrahigh-frequency (gigahertz) mechanical modes,[5,6] the technological implications of static deformation due to optical forces have been less explored.[7] In coupled photonic waveguide geometries,[8,9] bonding and anti-bonding optical modes are supported and the corresponding attractive and repulsive optical forces exerted on a pliant structure (low mechanical frequency) could serve to broaden the range of motion of integrated microelectromechanical devices. This translates to improvement in the detection range of pressure and displacement sensors and the actuation range of electrostatic actuators. In particular, the pull-in limit of electrostatic actuators could be extended by increasing the plate separation with a repulsive optical force. Additionally, schemes for preventing stiction, which occurs when attractive forces like the Casimir force and electrostatic force become overwhelmingly large compared to the mechanical restoring force, have been proposed[10] using a real-time monitoring of the structure's displacement and a counteracting feedback repulsive force (of the order of nano-Newtons and linear with excitation power). In this paper, we demonstrate nanometer-pulling of a thin silicon photonic crystal (PhC) membrane under low vacuum with a repulsive optical gradient force and an attractive photo-thermo-mechanical force. Furthermore, optical bistability induced by optical forces and thermo-optic effect is observed at large excitation powers.

Our devices, illustrated in Fig. 1(a), consist of a square silicon PhC slab suspended by four support arms ≈ 250 nm

above a Silicon-on-Insulator (SOI) substrate. They are fabricated (Fig. 1(b)) from a double-SOI platform, formed by oxide-oxide bonding of two thermally oxidized SOI wafers. A sacrificial silicon dioxide layer between the two silicon layers is $s_0 = 265$ nm thick. Electron-beam lithography is performed on a layer of resist (ZEP-520A) to define the pattern. To combat the strong buckling of the silicon device layer by the compressive stress and upward turning moments of the oxide layer underneath, stress management techniques[11,12] were incorporated to obtain structures with lithographically determined membrane-substrate gaps. After developing, a fluorine-based reactive-ion etch is employed to transfer the patterns to the top silicon layer. The device is then released by undercutting the patterned silicon layer with the vapor-phase hydrofluoric acid etch. Finally, an annealing step was performed at $500\,^\circ$C for 1 hour in a nitrogen environment to limit surface losses and maximize optical and mechanical quality factors. The separations of the released membranes from the substrate are characterized by a confocal microscope (Olympus LEXT OLS-4000).

The structure was designed to support an optical anti-bonding mode in the wavelength range of 1480–1680 nm, which results from the hybridization of waveguide modes in the membrane and substrate.[12,13] The precise spectral location of the resonance is determined by the optomechanical coupling between the two modes, the strength of which is defined as $g_{OM} \equiv d\omega/ds$, where ω is the optical resonant frequency. The distribution of the x-component of the electric field in the top membrane is out-of-phase from that in the bottom membrane, as depicted in the simulation results of the whole structure in Fig. 1(c), which corresponds to the generation of a repulsive gradient force. Additionally, the field symmetries along the x–z and y–z planes indicate that we are operating with a "dark" mode,[14] which theoretically does not couple to normally incident light because of mismatch in field symmetry. However, by breaking the periodicity of the
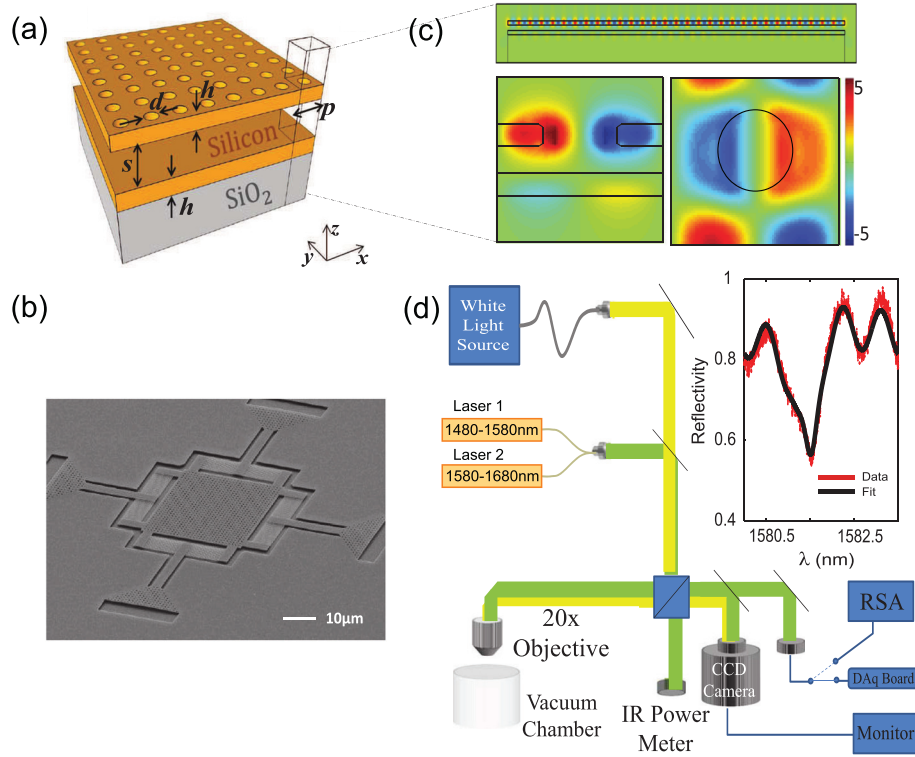
a)loncar@seas.harvard.edu.

FIG. 1. (a) Schematic of membrane geometry consisting of a suspended silicon membrane above a silicon-on-insulator substrate. The top membrane is perforated by a 30×30 array of holes with diameter $d = 0.414 \, \mu m$ and period $p = 0.92 \, \mu m$. Both silicon layers have thickness $h = 185 \, nm$. The width of the membrane is $27.6 \, \mu m$ on each side. (b) An electron micrograph of a device. (c) Top diagram shows the finite-difference time-domain (FDTD) simulated E_x field profile for the antibonding mode at $\lambda_0 = 1581.55 \, nm$ in the vertical cross-section of the full structure. Bottom left diagram shows the zoomed-in view of E_x field profile in the vertical cross-section of a unit cell. Bottom right diagram shows the E_x field profile in the horizontal cross-section of a unit cell, revealing the mode to be a dark mode. (d) Free-space coupling setup. A white-light source and output from a near-IR laser are combined and sent through a 50-50 beam splitter, sending half of the signal to an IR power meter and half through a $20\times$ objective placed above a vacuum chamber. The reflected signal is sent back through the beam splitter and can be directed onto a CCD camera allowing us to carefully align the laser spot to the membrane and to a photodetector (PD) to collect optical spectra via the DAq board and mechanical spectra via the real-time spectrum analyzer (RSA). Inset at right shows the reflection spectrum of the device around the resonance centered at $\lambda_0 = 1581.55 \, nm$.

full structure, we can couple to the dark mode and achieve high Q_{opt}.[15] Such devices have been the subject of numerous theoretical and experimental investigations on subjects ranging from the lowering of the laser thresholds[16] to increasing the sensitivity of photonic-crystal-based sensors.[17] Here, the dark mode is made accessible due to the finite size of the membrane and slight fabrication imperfection. The high Q_{opt} of the dark mode, together with the mode's large optomechanical coupling coefficient $g_{OM}/2\pi = -23 \, GHz/nm$ (at $s_0 = 220.6 \, nm$), boosts the strength of the optical force and hence the range of actuation. A low power ($25 \, \mu W$) wavelength sweep is shown in the inset of Fig. 1(d) (red curve) taken with a free-space resonance scattering setup in a low vacuum condition described in Fig. 1(d), revealing a cavity resonance centered at $\lambda_0 = 1581.55 \, nm$. To account for interference fringes from parasitic reflections, we carefully fit both the optical resonance and the oscillating background (black line) to an expression which has the form:

$$R = |r|^2 = \left| r_d(\lambda) e^{-i\phi} + \frac{\kappa_e}{-i\Delta_0 + \kappa/2} \right|^2, \quad (1)$$

where $r_d(\lambda)$ is the background reflectivity, ϕ is the relative phase between the underlying background reflection and the optical cavity, κ is the full-width half-max linewidth of the

optical resonance, κ_e is the external coupling rate. Δ_0 is the detuning (expressed in frequency) of the sweep wavelength from λ_0. Fitting parameters correspond to an optical cavity with $\kappa_e = 0.3 \, \kappa$ and $Q_{opt}^{tot} = \omega_0/\kappa = 3400$.

As previously described,[10] the potential of a mechanical harmonic oscillator with equilibrium position s_0, when perturbed by the potential of an optical "spring"[18] centered at s_l for a laser wavelength λ_l can create a multi-well potential with two stable mechanical equilibria. The transition between these mechanical equilibria is reflected by the occurrence of optical bistability, due to the dependence of the resonance frequency on s. Yet the direct observation of the optomechanically induced optical bistability can easily be obscured in actual systems by other competing mechanisms including the thermo-optic effect due to two-photon absorption, free-carrier dispersion, and the Kerr nonlinearity.[19] We designed our geometry to minimize these effects by exciting a guided resonance which is delocalized throughout the PhC membrane. We estimate the total mode volume to be $\approx 260(\lambda/n_g)^3$ from simulation. Due to its large modal volume, the thermal and electronic nonlinearities (which scale inversely with the modal volume) are dramatically reduced. This is in contrast with many of the optomechanical structures being studied, which have modal volumes $\approx (\lambda/n_g)^3$ and where thermal nonlinearities could be readily observed at even modest input

powers. Here, with the coupled PhC membrane of the current separations, optomechanical detuning is larger than thermo-optic detuning that originates from linear absorption due to defects introduced during the fabrication processes, which is two orders of magnitude larger than the intrinsic material absorption of bulk silicon.

We solve for the optical and mechanical equilibria in the presence of the thermo-optic effect within the coupled-mode theory framework.[20] In particular, the stored optical energy in the system $|a|^2$ is given by

$$|a|^2 = \frac{\kappa_e}{(\kappa/2)^2 + \Delta^2} P_{in}, \tag{2}$$

where P_{in} is the power incident on the structure, and κ_e/κ represents the fraction of incident power coupled into the cavity. The detuning Δ of the laser excitation frequency ω_l from the perturbed optical resonant frequency can be written as

$$\Delta = \omega_l - [\omega_0 + (d\omega/dT)\Delta T + g_{OM}\Delta x]. \tag{3}$$

The third term in Eq. (3) is the thermo-optic detuning, with $d\omega/dT = (d\omega/dn)(dn/dT)$, n is the refractive index of silicon, $d\omega/dn$ is obtained from simulations and approximately $-2\pi \times 10^{14}$ Hz, and dn/dT is the thermo-optic coefficient of silicon equal to 2×10^{-4} K^{-1}.[21] The absorbed optical power and hence the temperature change of the system is given by

$$\Delta T = \frac{\Gamma_{abs}|a|^2}{C_{th}\kappa_t}, \tag{4}$$

where Γ_{abs} is the absorption coefficient of the system, C_{th} is the heat capacity, and κ_t is the thermal diffusion rate. The fourth term in Eq. (3) is the optomechanical detuning. In particular, the displacement of the membrane due to the respective photo-thermo-mechanical force and the repulsive gradient force is given by

$$\Delta x = \frac{D\Delta T}{K} + \frac{|a|^2 g_{OM}}{\omega_l K}, \tag{5}$$

where K is the spring constant of the mechanical resonator and D is the thermal-mechanical force coefficient in units of Newtons per Kelvin.[22] We neglect the Duffing nonlinearity in our mechanical model as the extent of the optical actuation is still well within the linear regime for our structures: the amplitude is much less than the membrane thickness (185 nm) and the compressive stress in the silicon device layer is alleviated by thin accordion structures as shown in Fig. 1(b). The above equations can be solved self-consistently to yield Δ and hence the perturbed optical resonant frequency $\omega_0' = \omega_0 + (d\omega/dT)\Delta T + g_{OM}\Delta x$ at a given ω_l and P_{in}.

The values of $\lambda_0' = 2\pi c/\omega_0'$ at which solutions of Eq. (3) exist are plotted in Fig. 2, as a function of laser wavelength $\lambda_l = 2\pi c/\omega_l$ for incident powers of 0.275 mW (green line), 0.775 mW (blue line), 1.275 mW (red line), 1.525 mW (purple line), 1.775 mW (orange line), and 2.275 mW (black line). The unperturbed optical resonance occurs at

$\lambda_0 = 1581.55$ nm. The dashed portions of the curves correspond to unstable equilibria. At high powers, a clear bistable region exists in which there are two stable configurations of the membrane for fixed power and laser wavelength, due to both optomechanical and thermo-optic detunings whose magnitudes are comparable. The boundaries of the bistable region are denoted by λ_f and λ_b, representing the hysteretic transition wavelengths for a laser swept forward (left to right) and backward (right to left) across the resonance.

We can model the reflectance of the system as a function of laser wavelength at multiple powers ($P = 0.275$ mW to 2.275 mW—same powers as in Fig. 2) with Eq. (1) (with Δ_0 replaced by Δ_0') and the respective equilibria calculated in Fig. 2. The results are shown in Fig. 3(a) (offset for clarity), and are compared to our experimental observations shown in Fig. 3(b). The experimental data were collected by sweeping the tunable laser output from short to long wavelength (red curve) and then back (blue curve) at a fixed tuning speed of 1 nm/s. We find excellent agreement between experiment and theory, which displays an overall redshift of the mode and increasing hysteresis at higher powers. In particular, we directly compare the locations of the forward and backward bistable jumps, λ_f and λ_b, respectively, in Fig. 3(c). The locations of these transitions were extracted from the data shown in Fig. 3(b) by finding the minima of the reflectivities of forward and backward wavelength sweeps at each power. We see strong agreement between experiment (red/blue circles) and theoretical predictions from Eq. (3) (red/blue line) on the locations of λ_f and λ_b.
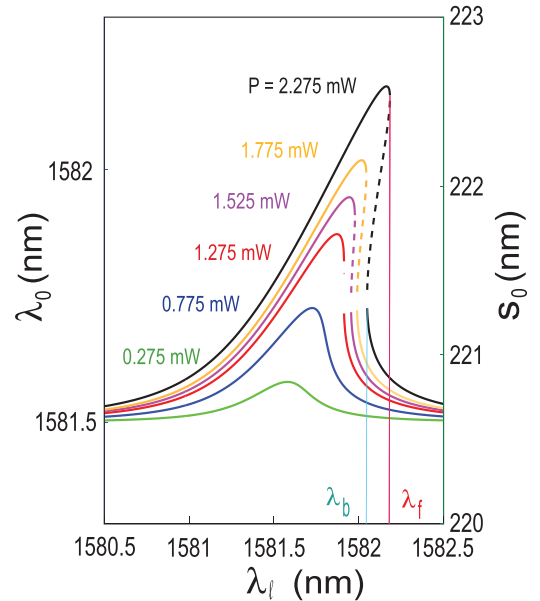

FIG. 2. Calculated stable locations of the optical resonance as a function of laser wavelength, for six optical powers: 0.275 (green line), 0.775 (blue line), 1.275 (red line), 1.525 (purple line), 1.775 (orange line), and 2.275 mW (black line). At $P \geq 1.275$ mW, the system has three solutions (two stable—solid line, one unstable—dashed line) for a certain range of wavelengths. Due to the intracavity-power dependence of optical detunings from optomechanical and thermo-optic effects, the system is bistable in this wavelength range and displays hysteresis when the laser is swept continuously from short to long wavelengths (forward sweep) or vice versa (backward sweep). Two hysteretic transition points occur at λ_f for the forward sweep and λ_b for the backward sweep.
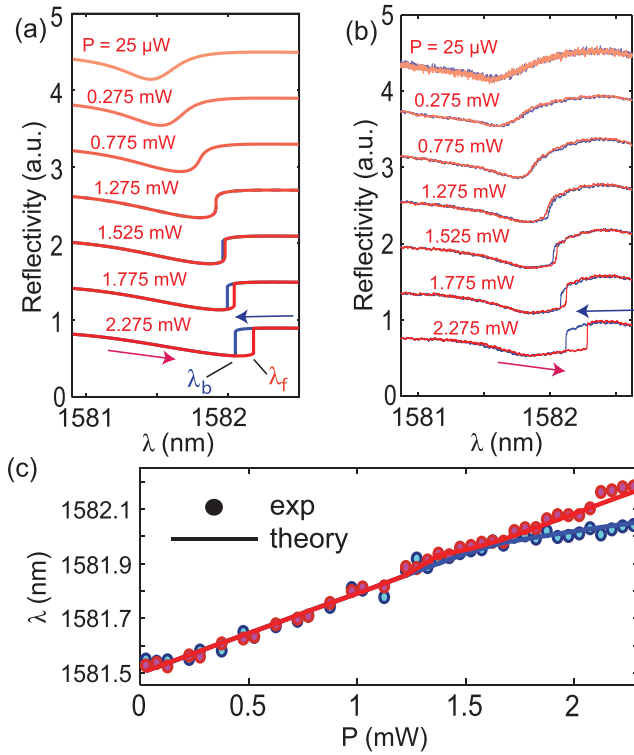
FIG. 3. Calculated (a) and experimental (b) reflection spectra for forward (red lines) and backward (blue lines) swept lasers from $P = 0.275$ mW to 2.275 mW at *low vacuum* ($\approx$10 mTorr). Hysteresis is predicted to onset around 1.525 mW. (c) Locations of bistable transitions during forward and backward wavelength sweeps. The transition wavelength during the forward sweep λ_f (red circles) is linear and matches well to calculations from Eq. (3) (red line). The backward transition wavelength λ_b (blue circles) also show good agreement in the transition wavelength locations and the onset power for hysteresis.
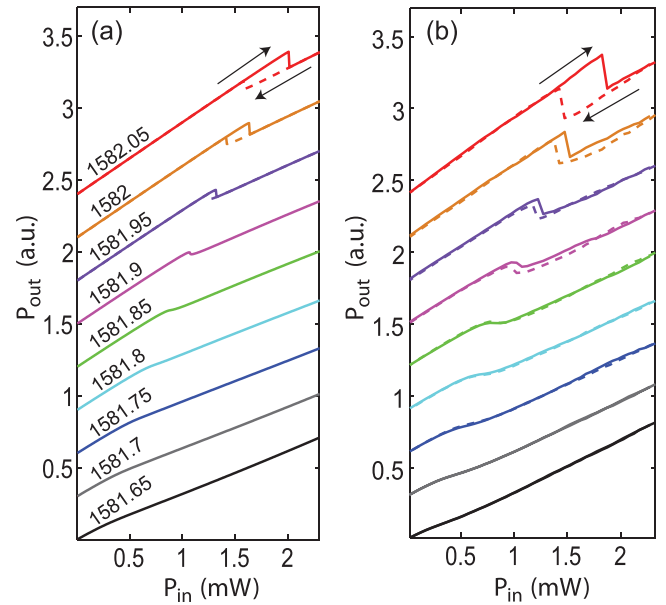

FIG. 4. Predicted (a) and experimental (b) P_{in}-P_{out} curves of the device. Curves (with equal vertical offsets for easier visualization) are plotted for five red-detuned wavelengths: $\lambda =$ 1581.65 nm (black line), 1581.7 nm (grey line), 1581.75 nm (blue line), 1581.8 nm (cyan line), 1581.85 nm (green line), 1581.9 nm (magenta line), 1581.95 nm (violet line), 1582 nm (brown line), and 1582.05 nm (red line). Solid lines represent the power output as a function of increasing laser power, while dashed lines represent power output as a function of decreasing input power. Modeling predicts hysteresis will occur at all wavelengths longer than 1581.95 nm.

Alternately, we can investigate the range of actuation of the optical force by sweeping the *laser power* up and down at fixed wavelengths slightly red-detuned from the unperturbed cavity resonance. Theoretical predictions and experimental results are plotted in Figs. 4(a) and 4(b), respectively, showing the reflected power plotted against the incident laser power at nine red-detuned wavelengths: 1581.65 nm (black line), 1581.7 nm (grey line), 1581.75 nm (blue line), 1581.8 nm (cyan line), 1581.85 nm (green line), 1581.9 nm (magenta line), 1581.95 nm (violet line), 1582 nm (brown line), and 1582.05 nm (red line). The curves for the eight longer wavelengths are each vertically offset from the $\lambda_l = 1581.65$ nm curves for clarity. Again, we see good agreement between the calculated and experimental results: For small detunings ($\lambda_l = 1581.65$ to 1581.9 nm), the path traversed during an increase in input power from 0 to 2.25 mW (solid line) and a decrease in power (dashed line) coincide. At larger detunings, P_{out} experiences hysteresis. As the power is increased, the membrane enters the bistable region in the lower mechanical state and remains there until λ_b has redshifted such that $\lambda_b = \lambda_l$, at which point the membrane jumps to the lower curve, signifying an abrupt increase in the membrane separation. When decreasing the power, the membrane remains in the up-state until λ_f blue-shifts back to λ_l, forcing the membrane to jump to the upper curve which indicates an abrupt hop back to the pulled initial equilibrium position.

When we decompose the perturbation to the optical resonance into its constituent parts, we find optomechanically induced bistability to be the dominant effect. For example, at $P_{in} = 2.275$ mW, optomechanical effects correspond to a peak resonance shift $\Delta\lambda_{OM} = 0.44$ nm, while thermo-optic contributions lead to $\Delta\lambda_{PT} = 0.23$ nm and photo-thermal-mechanical contributions lead to $\Delta\lambda_{PTM} = -0.01$ nm. This corresponds to a membrane which is mechanically pushed upward 2.3 nm by the optical gradient force and 0.1 nm downward by the photo-thermal-mechanical force, resulting in a net upward displacement of 2.2 nm. These results hold promise for large actuation range with repulsive optical forces by designing membranes which are less mechanically stiff and generate larger repulsive forces per mW of incident optical power by increasing Q_{opt}. For instance, Q_{opt} is currently limited by fabrication imperfections and the finite size effect of the PhC and could be boosted by simply increasing the number of unit cells in the membrane.[16] To maintain the same compactness of the structure which is related to its dynamic range, the optical design could be modified with a smaller lattice constant and/or graded hole modulation.[23]

In conclusion, we demonstrated actuation of a micron-scale membrane with a repulsive optical force using an extended guided resonance in a coupled silicon PhC membrane. The net red-shift displayed in the optical resonance of our doubly bonded SOI platform is a result of an optomechanically induced red-shift, a thermo-optic red-shift, and a photo-thermo-mechanically induced blue-shift. Furthermore, simulations indicate that absorption in our system is dominated by surface defects and adsorbents, resulting in a linear absorption coefficient two orders of magnitude larger than

that expected from bulk silicon. By minimizing these effects through fabrication process and design modifications, we can further isolate and exploit the unique optomechanical properties of this platform. Since multi-photon nonlinearities do not occur until the excitation power exceeds $\approx 1\,\mathrm{W}$ with the use of a delocalized optical mode, the extent of pulling of the PhC membrane can be many tens of nanometers. Our silicon-based device provides a simple, non-intrusive solution to extending the actuation range of MEMS devices.

[1]J. Chan, T. P. M. Alegre, A. H. Safavi-Naeini, J. T. Hill, A. Krause, S. Groblacher, M. Aspelmeyer, and O. Painter, Nature **478**, 89–92 (2011).

[2]A. G. Krause, M. Winger, T. D. Blasius, Q. Lin, and O. Painter, Nature Photon. **6**, 768–772 (2012).

[3]M. Hossein-Zadeh and K. J. Vahala, Appl. Phys. Lett. **93**, 191115 (2008).

[4]M. Davanco, J. Chan, A. H. Safavi-Naeini, O. Painter, and K. Srinivasan, Opt. Express **20**, 24394–24410 (2012).

[5]Y. T. Yang, C. Callegari, X. L. Feng, K. L. Ekinci, and M. L. Roukes, Nano Lett. **6**, 583–586 (2006).

[6]M. Eichenfield, R. Camacho, J. Chan, K. J. Vahala, and O. Painter, Nature **459**, 550–U79 (2009).

[7]G. S. Wiederhecker, L. Chen, A. Gondarenko, and M. Lipson, Nature **462**, 633–U103 (2009).

[8]M. L. Povinelli, M. Loncar, M. Ibanescu, E. J. Smythe, S. G. Johnson, F. Capasso, and J. D. Joannopoulos, Opt. Lett. **30**, 3042–3044 (2005).

[9]M. Li, W. H. P. Pernice, C. Xiong, T. Baehr-Jones, M. Hochberg, and H. X. Tang, Nature **456**, 480–U28 (2008).

[10]A. W. Rodriguez, D. Woolf, P. C. Hui, E. Iwase, A. P. McCauley, F. Capasso, M. Loncar, and S. G. Johnson, Appl. Phys. Lett. **98**, 194105 (2011).

[11]E. Iwase, P. C. Hui, D. Woolf, A. W. Rodriguez, S. G. Johnson, F. Capasso, and M. Loncar, J. Micromech. Microeng. **22**, 065028 (2012).

[12]D. N. Woolf, P. C. Hui, E. Iwase, M. Khans, A. W. Rodriguez, P. Deotare, I. Bulu, S. G. Johnson, F. Capasso, and M. Loncar, Opt. Express **21**, 7258–7275 (2013).

[13]A. W. Rodriguez, A. P. McCauley, P. C. Hui, D. Woolf, E. Iwase, F. Capasso, M. Loncar, and S. G. Johnson, Opt. Express **19**, 2225–2241 (2011).

[14]J. Lee, B. Zhen, S. L. Chua, W. J. Qiu, J. D. Joannopoulos, M. Soljacic, and O. Shapira, Phys. Rev. Lett. **109**, 067401 (2012).

[15]O. Kilic, M. Digonnet, G. Kino, and O. Solgaard, Opt. Express **16**, 13090–13103 (2008).

[16]S. L. Chua, Y. D. Chong, A. D. Stone, M. Soljacic, and J. Bravo-Abad, Opt. Express **19**, 1539–1562 (2011).

[17]M. El Beheiry, V. Liu, S. H. Fan, and O. Levi, Opt. Express **18**, 22702–22714 (2010).

[18]B. S. Sheard, M. B. Gray, C. M. Mow-Lowry, D. E. McClelland, and S. E. Whitcomb, Phys. Rev. A **69**, 051801 (2004).

[19]P. B. Deotare, I. Bulu, I. W. Frank, Q. M. Quan, Y. N. Zhang, R. Ilic, and M. Loncar, Nat. Commun. **3**, 846 (2012).

[20]T. J. Kippenberg and K. J. Vahala, Opt. Express **15**, 17172–17205 (2007).

[21]T. J. Johnson, M. Borselli, and O. Painter, Opt. Express **14**, 817–831 (2006).

[22]D. Blocher, A. T. Zehnder, R. H. Rand, and S. Mukerji, Finite Elem. Anal. Design **49**, 52–57 (2012).

[23]K. Srinivasan and O. Painter, Opt. Express **10**, 670–684 (2002).